PNAS RESEARCH ARTICLE | MEDICAL SCIENCES

Distinct transcription factor interactions drive HOXB13 activity in different stages of prostate cancer

Betul Ersoy-Fazlioglu[a,b,1], Shreyas Lingadahalli[c,1], Umut Berkay Altintas[c], Ahmet Cingoz[a,b], Emirhan Tekoglu[a,b], Ivan Pak Lok Yu[c], Meric Dikbas[c], Olka Missaghimamaghani[c], Kerim Yavuz[c], Hans Adomat[c], Ibrahim Kulac[b], Tunc Morova[c], Kevin Xiao[c], Martin Gleave[c,d], Ladan Fazli[c], Paloma Cejas[e], Artem Cherkasov[c,d], Wilbert Zwart[f,g], Michael Christoph Haffner[h,i,j], Henry W. Long[e], Colin Collins[c,d], Tugba Bagci-Onder[a,b], and Nathan A. Lack[a,b,c,d,2]

Affiliations are included on p. 11.

Edited by Arul Chinnaiyan, University of Michigan Medical School, Ann Arbor, MI; received January 6, 2025; accepted October 20, 2025

HOXB13 is a lineage-specific transcription factor that plays a critical role in initiation and progression of prostate cancer (PCa). While most research has focused on the role of HOXB13 on androgen receptor (AR) activity, here we demonstrate that HOXB13 is frequently expressed in AR-negative tumors and is essential for the proliferation of both AR-positive and -negative PCa models. Strikingly, HOXB13 is remarkably selective and has almost no effect on nonprostatic tissues. Despite this common essentiality in PCa, HOXB13 activity is markedly different in AR-negative stem cell–like tumors, where interactions with the AP-1 change the HOXB13 cistrome and interactome. Yet despite these distinct activities, HOXB13 activity is commonly mediated by SMARCD2, a member of the mSWI/SNF chromatin remodeling complex. The HOXB13/SMARCD2 interaction alters chromatin accessibility at HOXB13-binding sites, causing increased proliferation in AR-negative PCa. Overall, this work demonstrates a distinct mechanism of action for HOXB13 and highlights its critical role in AR-negative castration-resistant PCa.

HOXB13 | mSWI/SNF | prostate cancer | androgen receptor

Significance

HOXB13 is a lineage-specific transcription factor essential for prostate cancer (PCa) proliferation in both androgen receptor (AR)-positive and AR-negative tumors, with minimal effects on nonprostatic tissues. In AR-negative, stem-like PCa, HOXB13 interacts with AP-1, reshaping its cistrome and interactome. Despite interacting with different transcription factors during PCa progression, cellular activity was found to converge on SMARCD2, a chromatin remodeling complex subunit, and drive tumor proliferation via altered chromatin accessibility. This study uncovers a distinct mechanism for HOXB13 in AR-negative castration-resistant PCa, emphasizing its potential as a therapeutic target.

Prostate cancer (PCa) is the second leading cause of cancer-related death in North American men (1). Androgen receptor (AR) pathway inhibitors (ARPI) are the standard of care to treat recurrent or metastatic PCa. However, the clinical response to ARPIs is only temporary, and most patients progress to lethal castration-resistant PCa (CRPC) (2, 3). Although the majority of these CRPC tumors continue to rely on AR signaling, a subset of PCa (~20%) no longer depend on AR activity (4–6). As compared to AR-positive adenocarcinoma, these AR-negative/low PCa tumors have considerable diversity leading to several distinct classifications including treatment-induced neuroendocrine (t-NEPC), stem cell–like and double negative PCa (5, 7). Despite the approval of new therapeutics, both AR-positive and -negative/low CRPC are almost universally lethal.

Prostate embryogenesis is mediated through the expression of posterior homeotic (HOX) genes including *HOXD13*, *HOXC13*, and *HOXB13* (8–10). Unlike most HOX genes that are expressed only during development, *HOXB13* remains highly transcribed in the adult prostate where it is believed to play a role in maintaining cellular identity (8). There is extensive clinical and experimental evidence that HOXB13 contributes to PCa development. Several *HOXB13* germline variants, including G84E, have been associated with increased PCa frequency, Gleason scores, and a greater likelihood of positive surgical margins at the time of radical prostatectomy (11–14). HOXB13 expression does not significantly change during PCa development and is proposed to contribute to neoplastic transformation through alterations in coregulatory protein interactions. During PCa progression, HOXB13 transitions from interacting with the tumor suppressor three-amino acid loop extension protein, MEIS1, to the oncogenic AR (15–17). This interaction dramatically changes AR cistrome leading to locus-specific changes in AR-mediated transcription that contribute to PCa development and growth (18, 19). HOXB13 also interacts with constitutively active AR splice variants and alters both DNA binding and transcription of target oncogenes (20). Additionally, HOXB13 has an AR-independent function that modulates lipogenesis in AR-positive PCa (21). While there is a clear relationship between HOXB13 and AR, recent work has demonstrated that HOXB13 remains highly expressed in the majority of AR-negative PCa (22). Yet it is unclear if or how HOXB13 contributes to the growth of these AR-negative tumors.

In this study, we demonstrate that HOXB13 is commonly expressed in both AR-positive and -negative CRPC and may represent a potential mechanism to bypass AR dependencies. We show that HOXB13 is critical to growth and proliferation of nearly all AR-positive and -negative PCa models. Notably, exogenous *HOXB13* expression significantly increases the

Preprint Server: This manuscript was deposited to bioRxiv under a CC-BY-ND 4.0 International license (https://doi.org/10.1101/2023.09.04.556101).

Author contributions: B.E.-F., S.L., M.G., T.B.-O., and N.A.L. designed research; B.E.-F., S.L., A. Cingoz, I.P.L.Y., M.D., O.M., K.Y., H.A., and K.X. performed research; B.E.-F., S.L., U.A., A. Cingoz, E.T., I.K., T.M., L.F., P.C., A. Cherkasov, W.Z., M.C.H., H.W.L., C.C., T.B.-O., and N.A.L. analyzed data; and B.E.-F., S.L., and N.A.L. wrote the paper.

The authors declare no competing interest.

This article is a PNAS Direct Submission.

Copyright © 2025 the Author(s). Published by PNAS. This article is distributed under Creative Commons Attribution-NonCommercial-NoDerivatives License 4.0 (CC BY-NC-ND).

[1]B.E.-F. and S.L. contributed equally to this work.

[2]To whom correspondence may be addressed. Email: nlack@prostatecentre.com.

This article contains supporting information online at https://www.pnas.org/lookup/suppl/doi:10.1073/pnas.2500327122/-/DCSupplemental.

Published December 4, 2025.

Downloaded from https://www.pnas.org by KOC UNIVERSITY LIBRARY on June 1, 2026 from IP address 88.255.99.32.

proliferation rate of *HOXB13*-null PCa cells. While commonly essential, HOXB13 activity dramatically changes during progression and transitions from interactions with AR in models of adenocarcinoma to interactions with AP-1 transcription factors in AR-negative/low PCa. Yet despite the diverse transcription factor interactions, HOXB13 activity is commonly mediated by SMARCD2, a member of the mSWI/SNF chromatin remodeling complex. This HOXB13/SMARCD2 interaction is stabilized by cell-specific transcription factors, which alters chromatin accessibility at HOXB13-binding sites and causes increased proliferation in PCa.

Results

HOXB13 Remains Expressed in AR-Independent Cancers. To investigate the relationship between HOXB13 and AR expression in PCa, we conducted immunohistochemistry in multiple clinical cohorts. We found that HOXB13 is highly expressed in primary PCa, adenocarcinoma CRPC, and AR-positive t-NEPC (Fig. 1 *A* and *B*). While there was a loss or reduction of HOXB13 expression in some AR-negative t-NEPC clinical samples (4/7) (23), we observed that many tumors (3/7) still continued to express medium to high levels of HOXB13 (Fig. 1*B*). Looking at publicly available RNA-seq of an independent CRPC cohort (24), we found that *HOXB13* mRNA expression was reduced but still expressed in many AR-negative tumors (Fig. 1*C*). A larger cohort of 483 AR+ and 113 AR- tumor samples from a total of 52 CRPC patients similarly showed that HOXB13 was maintained in many AR- patients (Fig. 1*D* and *SI Appendix*, Fig. S1*A*). Additional multiplex immunofluorescence of t-NEPC tumors also supports our earlier IHC and demonstrates that some, but not all t-NEPC cancer cells coexpress HOXB13 (*SI Appendix*, Fig. S1*B*). Overall, our findings demonstrate that some AR-negative tumors still continue to express HOXB13. When looking at *HOXB13* expression in published patient-derived xenografts (PDX) of AR-low/negative CRPC tumors, we found high expression of *HOXB13* in both t-NEPC and stem cell–like CRPC, but almost none in WNT-driven CRPC (7) (Fig. 1*E*). As some work has suggested that HOXB13 expression is driven by AR activity (25–27), we characterized HOXB13 expression following inhibition of AR with ARPI in a neoadjuvant primary PCa cohort (*SI Appendix*, Fig. S1*C*). We found inhibiting AR with androgen deprivation therapy did not significantly decrease HOXB13 expression, supporting that expression of this protein is independent of AR. Overall, these findings show that HOXB13 is commonly expressed in AR-low/negative CRPC patients.

HOXB13 Is Essential for the Growth of AR-Negative PCa. To explore the role of HOXB13 in late-stage PCa, we knocked out *HOXB13* in vitro with CRISPR/Cas9 using three separate sgRNAs in androgen-dependent PCa cell lines (LNCaP, VCaP, 22Rv1); androgen-independent AR-positive PCa cell lines (LNAI, LNCaP ABL); AR-negative PCa cell line (PC3); and non-PCa cell lines (293T, Hep3B). In all HOXB13-expressing PCa cell lines (*SI Appendix*, Fig. S2*A*), CRISPR/Cas9 knockout significantly decreased cell proliferation while it had minimal effect on non-PCa cell lines (Fig. 2*A* and *SI Appendix*, Fig. S2*B*). Strikingly, the effect on proliferation was independent of AR expression, as the AR-negative PC3 cell line was the most sensitive to HOXB13 knockout. This phenotype was not due to guide RNA off-target effect, as we observed similar effects on proliferation with

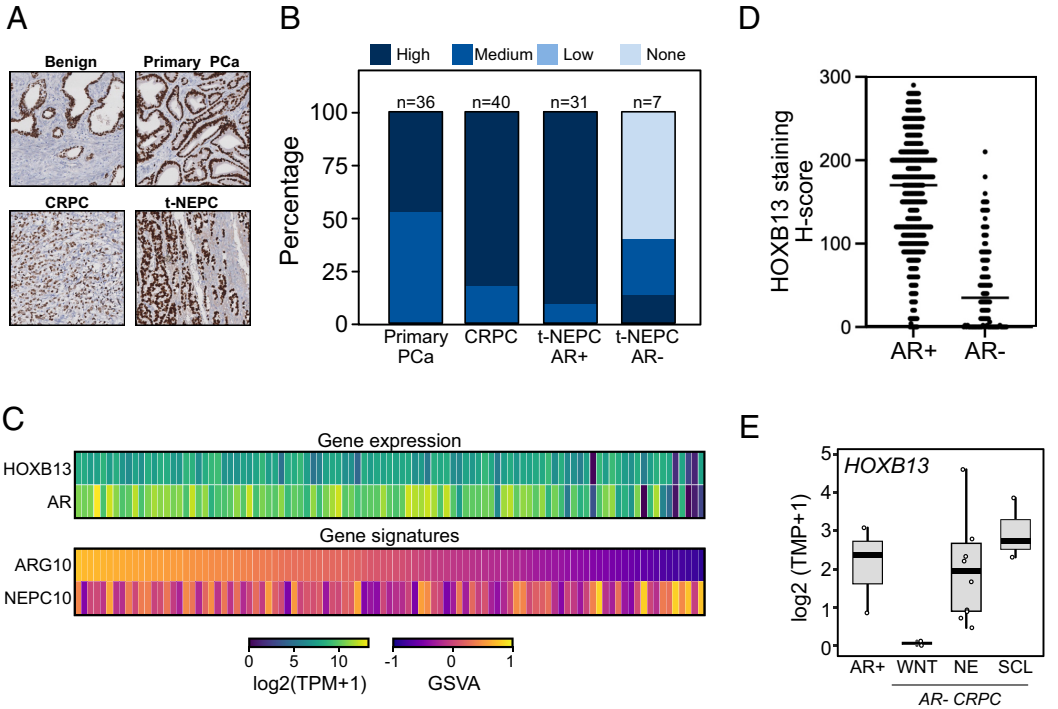


Fig. 1. HOXB13 expression is independent of AR. (*A*) HOXB13 expression was evaluated by IHC in a tissue microarray containing primary PCa, adenocarcinoma CRPC, AR-positive (AR+) t-NEPC, and AR-negative (AR-) t-NEPC (n = 114). (*B*) HOXB13 expression from the TMA IHC was graded by a clinical pathologist as high, medium, low, or no HOXB13 expression. HOXB13 expression reduced, but still commonly found in many AR- t-NEPC tumors (*C*) *HOXB13* and *AR* expressions were quantified from publicly available RNA-seq of laser-capture microdissected CRPC tumor tissue (n = 99) and compared to published AR and NEPC gene signatures (ARG10 and NEPC10, respectively). (*D*) To validate our initial observations, we analyzed HOXB13 expression in a larger cohort comprising 596 tumor samples from 52 patients (n = 483 AR+; n = 113 AR- tumors). Similar to earlier work we observed that HOXB13 expression was preserved in a substantial fraction of AR-negative (AR-) tumors. (*E*) HOXB13 expression was compared in AR-positive and -negative CRPC subtypes (7) including AR-positive adenocarcinoma (CRPC-AR), AR-negative WNT-driven CRPC (CRPC-WNT), AR-negative neuroendocrine PCa (CRPC-NE), and AR-negative stem cell–like CRPC (CRPC-SCL). High expression was observed in CRPC-AR, CRPC-NE, and CRPC-SCL while no expression was observed in WNT-driven CRPC.

Downloaded from https://www.pnas.org by KOC UNIVERSITY LIBRARY on June 1, 2026 from IP address 88.255.99.32.

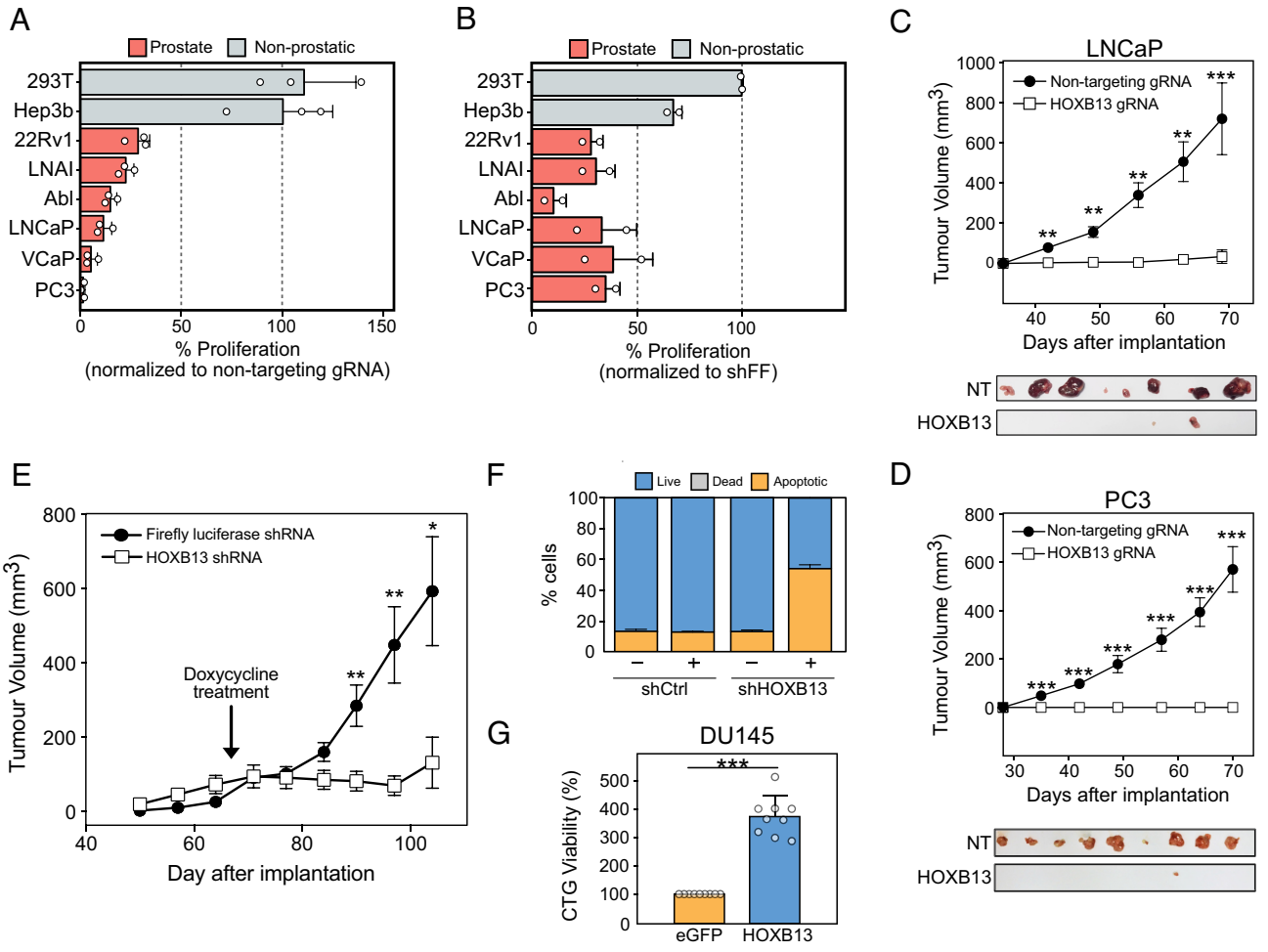


Fig. 2. HOXB13 is selectively essential to nearly all PCa models. (*A*) Proliferation assay in PCa and nonprostatic cell lines with *HOXB13* knockout via CRISPR/Cas9 gene editing (n = 3; mean ± SEM). (*B*) shRNA knockdown shows selective essentiality for HOXB13 in PCa (n = 4 as biological replicates; mean ± SEM). (*C*) Tumor growth in vivo characterizing the effect of HOXB13 on PCa initiation in AR-dependent (n = 8; mean ± SEM) and (*D*) AR-independent (n = 15; mean ± SEM) subcutaneous xenografts. (*E*) Tumor growth in vivo characterizing the effect of HOXB13 in PCa progression (n = 20; mean ± SEM unpaired two-tailed *t* test). shHOXB13 and shFF were induced with doxycycline once tumors became palpable. (*F*) Annexin V staining demonstrating that HOXB13 loss induces apoptosis in LNCaP model (n = 3; mean ± SEM). (*G*) Proliferation assay in *HOXB13*-null PCa (DU145) shows increased growth following HOXB13 overexpression (n = 9; mean ± SEM; unpaired two-tailed *t* test). For all experiments, an unpaired two-tailed *t* test was used (ns $P > 0.05$, *$P < 0.05$, **$P < 0.01$, ***$P < 0.001$).

shRNA targeting *HOXB13* (n = 4) (Fig. 2*B* and *SI Appendix*, Fig. S3 *A* and *B*). When we quantified *HOXB13* dependency from published genome-wide CRISPR screens [DepMap 22Q1; (28)] we found that *HOXB13* knockout was highly selective to PCa cell lines and did not significantly impact the proliferation of nearly all nonprostatic cell lines (1059/1061) (*SI Appendix*, Fig. S4). Building on these in vitro results, we then tested the impact of HOXB13 on AR-negative in vivo xenograft initiation and growth. To characterize the impact of HOXB13 on tumor initiation, we knocked out *HOXB13* and generated subcutaneous xenografts in both AR-positive (LNCaP) and AR-negative (PC3) models. To obtain enough viable cells to generate xenografts after *HOXB13* knock out, we transduced a large number of cells and initiated subcutaneous engraftment immediately after antibiotic selection. In these models, loss of HOXB13 caused a near total inhibition of PCa engraftment, and almost no tumors could be observed (Fig. 2 *C* and *D*). Next, we tested how HOXB13 impacted proliferation in engrafted tumors. In this, subcutaneous xenografts were generated with PC3 cells stably expressing inducible shRNA against either *HOXB13* (shHOXB13) or firefly luciferase (nontargeting shCtrl) (*SI Appendix*, Fig. S5 *A* and *B*). Once a palpable tumor (volume ~100 mm^3) was detected, shRNA expression was induced with exogenous doxycycline. No difference was observed in growth of shHOXB13 and shCtrl xenografts before doxycycline treatment. However, following RNAi induction, those tumors expressing shHOXB13 showed a significant reduction in tumor size compared to the shCtrl group (Fig. 2*E*). When we characterized the mechanism of cell death in vitro by Annexin V staining, we found that loss of HOXB13 caused acute cell death in PCa by cellular apoptosis (Fig. 2*F*). Overall, these results demonstrate that HOXB13 is essential for both in vivo tumor initiation and growth of AR-negative PCa.

Effect of HOXB13 Overexpression in AR-Negative Models. Having demonstrated that HOXB13 was essential in PCa models, we then tested the effect of overexpression. Similar to previous work, we found that *HOXB13* overexpression was profoundly toxic on those AR+ cells that were dependent on HOXB13 (29) (*SI Appendix*, Fig. S6*A*). However, when we expressed HOXB13 in DU145, an AR-negative PCa cell line that does not express *HOXB13*, we observed significantly increased cellular growth (Fig. 2*G*). Suggesting that it was not an artifact of the assay, we saw a similar phenotype in several orthogonal cell proliferation assays (*SI Appendix*, Fig. S6 *B–D*). Interestingly, unlike AR+ adenocarcinoma models, *HOXB13* overexpression did not cause any toxicity in AR- HOXB13+ PC3 cells (*SI Appendix*, Fig. S6*E*).

Downloaded from https://www.pnas.org by KOC UNIVERSITY LIBRARY on June 1, 2026 from IP address 88.255.99.32.

Growth effect was specific to DU145, and overexpression of HOXB13 in a nonprostatic cell line (HEK293T) had no effect on cellular growth either (*SI Appendix*, Fig. S6 *F* and *G*). These data show that HOXB13 expression selectively promotes PCa growth.

HOXB13 has Distinct Chromatin Binding in AR-Negative PCa. There is extensive work demonstrating that HOXB13 colocalizes at AR-binding regions (ARBS) on DNA and affects AR-mediated transcription (18, 19). However, as we demonstrated that HOXB13 is both commonly expressed in AR-negative tumors and essential for proliferation in AR-negative cells, we reasoned that HOXB13 could potentially interact with alternative transcription factors in a cell-specific manner. To identify these transcription factors, we characterized the HOXB13 cistrome in both AR-positive (LNCaP) and AR-negative (PC3) cells by chromatin immunoprecipitation followed by sequencing (ChIP-seq) (Fig. 3*A*). We observed striking differences in HOXB13-binding sites (HXBS) in these cell lines with minimal overlap in the HOXB13 cistrome (<10%) (Fig. 3 *A*–*C*). The HOXB13 DNA-binding motif was centrally enriched at both LNCaP- and PC3-specific HXBS (*SI Appendix*, Fig. S7*A*). Strong HOXB13 binding was seen in LNCaP cells at *cis*-regulatory elements of AR-regulated genes, while no binding was observed at these regions in PC3 cells (Fig. 3*B*). Ranked motif analysis showed that HXBS in AR-positive cells were enriched for AR and coregulators motifs such as AR, FOXA1, and GATA2, while AR-negative cells were enriched for AP-1 (JUN/FOS) transcription factor (Fig. 3*D*).

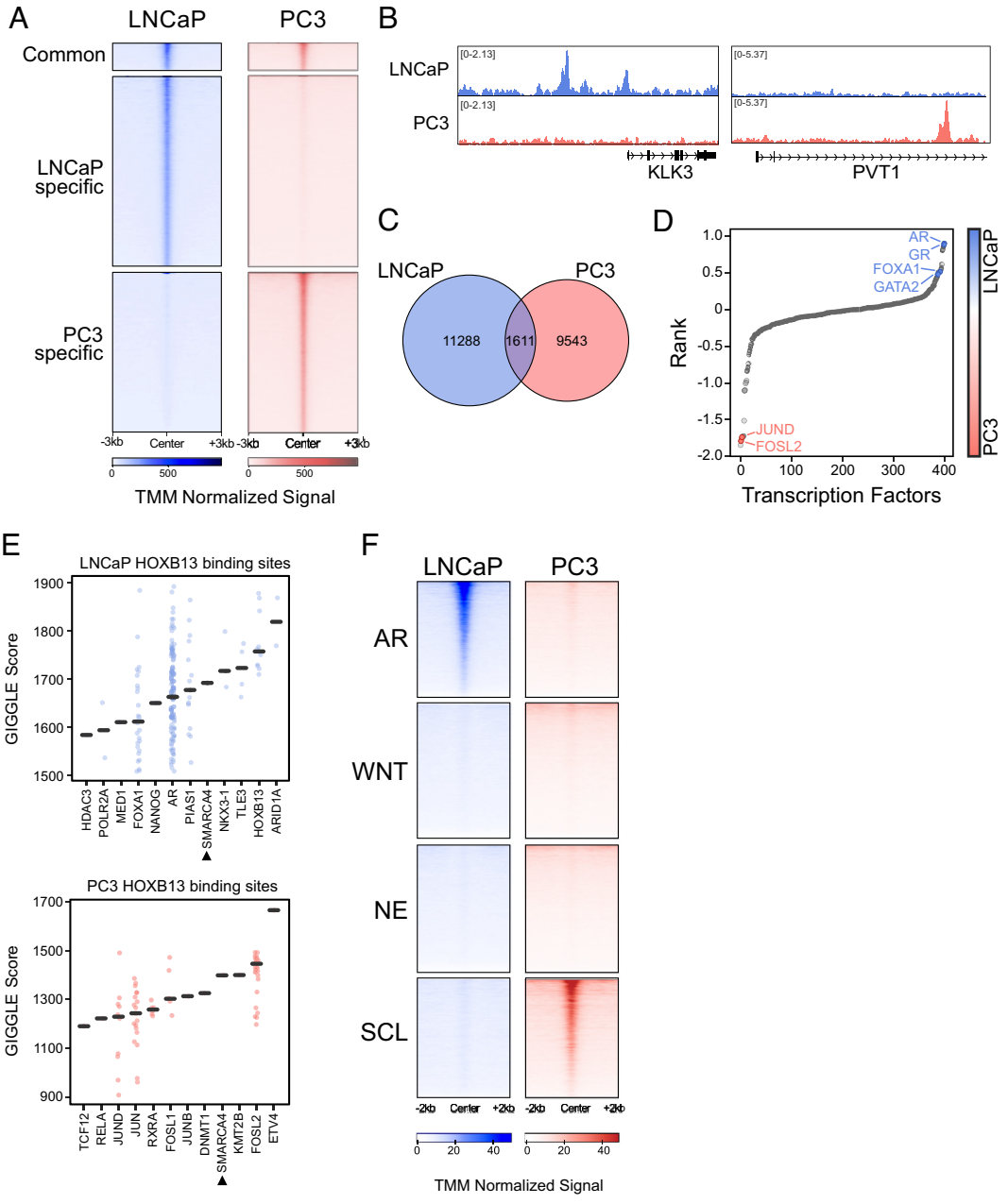


Fig. 3. HOXB13 has a distinct cistrome in different stages of prostate cancer (PCa). (*A*) Heatmap of sorted TMM normalized HOXB13 ChIP-seq signal in LNCaP and PC3 cells. (*B*) HOXB13 has distinct binding patterns in LNCaP and PC3 cells. (*C*) HOXB13-binding sites show minimal overlap (<10%) between LNCaP and PC3 cells. (*D*) Motifs ranked on their enrichment in LNCaP (Blue) and PC3 (Red) cells. (*E*) GIGGLE score of TFs shows SMARCA4 to be enriched at HOXB13-binding sites in both LNCaP (*Top*) and PC3 (*Bottom*) cells. (*F*) HOXB13 ChIP-seq signal from LNCaP and PC3 cells on PDX subtype-specific chromatin accessibility. HOXB13 binding was compared to ATAC-seq from AR-positive adenocarcinoma (AR), AR-negative WNT-driven CRPC (WNT), AR-negative neuroendocrine PCa (NE), and AR-negative stem cell–like CRPC (SCL). LNCaP-HXBS is enriched in CRPC-AR and PC3-HXBS in SCL-CRPC with no overlap in their binding.

Downloaded from https://www.pnas.org by KOC UNIVERSITY LIBRARY on June 1, 2026 from IP address 88.255.99.32.

Comparison of HOXB13 cistromes with published ChIP-seq studies using GIGGLE (30) showed that LNCaP HXBS significantly overlapped with AR cofactors including ARID1A, FOXA1, and NKX3-1 (Fig. 3*E*). In contrast, analysis of HXBS in AR-negative PC3 cells showed significant overlap with AP-1 (JUN/FOS) and ETV4 (7). Despite these differences we observed a common overlap of SMARCA4, a member of the mSWI/SNF complex. The overlap with AP-1-binding sites was particularly interesting, as recent work had identified a stem cell–like (SCL) AR-low/negative CRPC subset that is driven by this transcription factor (7). We observed a marked difference in transcription factor motifs at HXBS with LNCaP-specific sites showing an enrichment for AR androgen response elements, while PC3-specific sites had an enrichment for FOSL2 motifs, a component of AP-1 complex. These results suggest that a direct, motif-dependent, engagement by HOXB13 is a key mechanism for targeting unique regulatory elements in AR-negative CRPC. To explore the potential role of HOXB13 in late-stage PCa, we mapped HXBS cistromes to published ATAC-seq from AR-positive and -low/negative CRPC subtypes (Fig. 3*F*). We saw a significant overlap with LNCaP HOXB13 cistrome and AR-dependent CPRC. Strikingly, the PC3 HOXB13 cistrome was highly enriched in AP-1-driven AR-low/negative SCL-CRPC, suggesting that HOXB13 interacts with this transcription factor in AR-negative tumors. To address the suitability of PC3 as a model of AR-negative SCL-CRPC tumors, we analyzed published RNA-Seq and ATAC-seq of Patient Derived Organoids and Xenografts (7). Similar to the original study, we observed that PC3 cells closely phenocopy the SCL-CRPC tumors (*SI Appendix*, Fig. S7 *B* and *C*). Overall, these results suggest that HOXB13 distinctly interacts with AP-1 in AR-negative SCL-CRPC.

Defining the HOXB13 Interactome in AR-Negative PCa. HOX proteins regulate gene transcription in a tissue-specific manner through protein–protein interactions (31). Given the large differences we observed in DNA binding, we hypothesized that there would be a cell-specific HOXB13 interactome in AR-positive and -negative PCa. To characterize these differences, we performed HOXB13 Rapid Immunoprecipitation Mass Spectrometry (RIME) in both AR-positive (LNCaP and 22Rv1) and AR-negative (PC3) PCa models (n = 3; Fig. 4*A*). High HOXB13 peptide coverage was seen across all RIME biological repeats and cell lines (~40%) with no HOXB13 peptides in IgG controls (Fig. 4*B*). Using a conservative threshold (log2 fold change HOXB13/IgG > 2 and $P < 0.05$), we identified 73, 123, and 153 high-confidence HOXB13-interacting proteins in LNCaP, 22Rv1, and PC3 cells, respectively (Fig. 4*C* and *SI Appendix*, Table S4). While each cell line had a distinct HOXB13 interactome, there were marked differences between AR-positive and -negative cell lines. Specifically, most HOXB13-interacting proteins that were commonly found in both LNCaP and 22Rv1 were components of the AR-transcriptional complex including AR, FOXA1, and NKX3-1 (Fig. 4*C*). In contrast, the HOXB13 interactome in AR-negative PC3 was markedly different and, similar to our ChIP-seq analysis, showed selective AP-1 interactions (cJUN). Despite unique HOXB13–transcription factor interactions

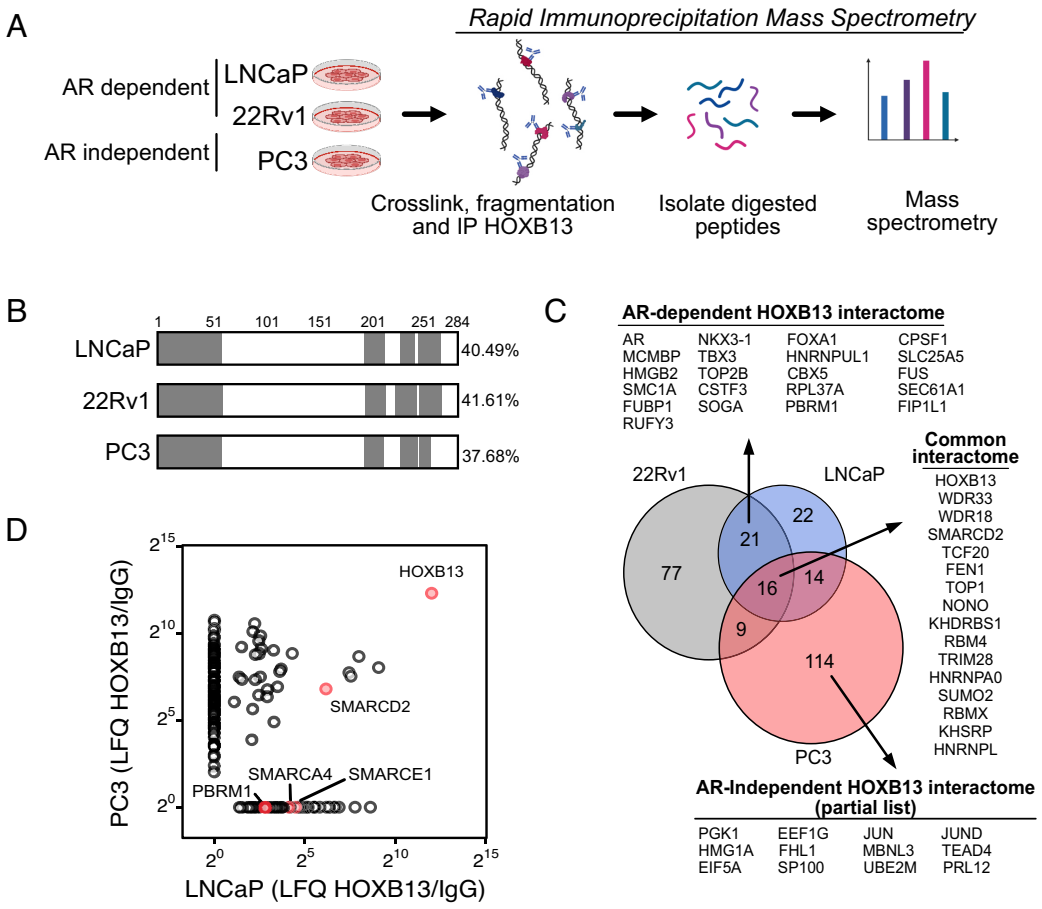


Fig. 4. HOXB13 has a unique interactome in AR-positive and AR-negative models. (*A*) Schematic representation of HOXB13-RIME. (*B*) Average peptide coverage of HOXB13 from individual RIME experiments in different cell lines. (*C*) HOXB13 interactome shows minimum overlap in AR-positive and AR-negative PCa models. More than 50% of the HOXB13-interacting proteins are common to both LNCaP and 22Rv1 cells and are known AR coregulators. (*D*) Many of the HOXB13-interacting proteins in AR-positive (LNCaP) and AR-negative (PC3) were markedly distinct. Members of the mSWI/SNF complex and HOXB13 are highlighted in red.

Downloaded from https://www.pnas.org by KOC UNIVERSITY LIBRARY on June 1, 2026 from IP address 88.255.99.32.

in AR-positive and -negative models, we reasoned that there could be a common effector function that drives HOXB13 activity. Metascape analysis for biological functional enrichment of HOXB13 interacting proteins showed significant enrichment for RNA splicing and chromatin modifications in all models (32) (Fig. 4*D*), including several members of the mSWI/SNF chromatin remodeling complex (SMARCA4, SMARCA2, SMARCE1, ARID1A, SMARCD2, and PBRM1 (Fig. 4*E*). The mSWI/SNF complex is a key regulator of nucleosome positioning and contains several core, ATPase catalytic, and variable subunits to provide a distinct identity to each complex (33). This was supported by our ChIP-seq results, where both motif and GIGGLE analysis from AR-positive and -negative models demonstrated that both HOXB13 cistromes were commonly enriched for mSWI/SNF subunits (Fig. 3*E*). While we observed various mSWI/SNF subunits in each interactome, SMARCD2 was found to interact with HOXB13 in all cell lines (Fig. 4*C*). These experiments provide evidence that while HOXB13 selectively interacts with the AP-1 complex in AR-negative CRPC, there may be a common effector with AR-positive PCa through the mSWI/SNF complex in PCa.

Characterizing the HOXB13–SMARCD2 Interaction. As previous studies have suggested, HOXB13 can function as a pioneer factor that preferentially binds to specific CpG-methylated DNA (34), we reasoned that HOXB13 activity can be commonly mediated by the mSWI/SNF chromatin-modifying complex. To validate the interactions between HOXB13 and SMARCD2, we performed in situ proximity ligation assay (PLA) in multiple PCa cell lines (LNCaP, 22Rv1, PC3, and DU145). A strong PLA signal was seen in all cells except DU145, which does not express endogenous HOXB13 (Fig. 5 *A* and *B*). Demonstrating the selectivity of this approach, when we overexpressed HOXB13 in DU145 cells, we could observe an interaction with SMARCD2 (Fig. 5*C*). This HOXB13–SMARCD2 interaction was confirmed by coimmunoprecipitation (CoIP) in cells exogenously expressing Flag-HOXB13 and Myc-His-SMARCD2 (Fig. 5*D*). To determine whether SMARCD2 co-occupies HOXB13-binding sites in PCa cells, we conducted SMARCD2 ChIP-seq (Fig. 5*E*) and observed a significant overlap between HOXB13 and SMARCD2 cistromes in LNCaP cells. Interestingly, HOXB13–SMARCD2 overlapping sites were significantly enriched at AR-binding sites as compared to HOXB13-alone sites (Fig. 5 *E* and *F*).

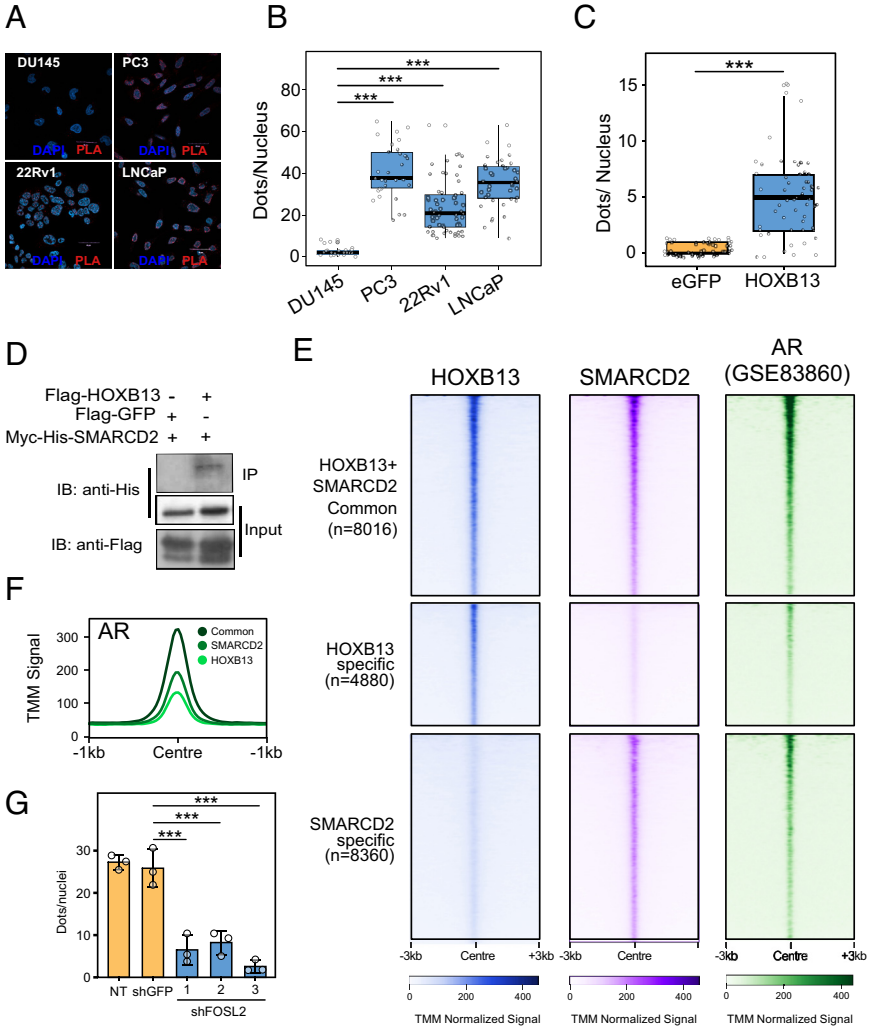


Fig. 5. SMARCD2 interacts with HOXB13. (*A*) Representative confocal image of HOXB13–SMARCD2 interactions quantified by in situ PLA. (*B*) HOXB13–SMARCD2 interactions were quantified manually and represented as dots/nuclei. The box plot represents results from 3 independent experiments (4 random 100X microscopy fields per experiment), and each dot represents an individual nucleus. (*C*) DU145 cells were transfected with either eGFP or HOXB13. In situ PLA shows significant HOXB13–SMARCD2 interactions only in DU145 cells expressing HOXB13. (*D*) CoIP in HEK293 cells cotransfected with Myc-His-SMARCD2 and Flag-HOXB13 or Flag-GFP. IP with anti-Flag antibody was probed with anti-His antibody. (*E*) Heatmap of sorted TMM normalized ChIP-seq peaks of HOXB13, SMARCD2, and AR in LNCaP cells. SMARCD2 was found to co-occupy those HXBS that were bound by AR. (*F*) HOXB13–SMARCD2 overlapping sites were significantly enriched at AR-binding sites as compared to the HOXB13 alone or SMARCD2 alone sites. (*G*) shRNA knockdown of the AP-1 component *FOSL2* in PC3 cells reduced the interactions between HOXB13 and SMARCD2. For all data ns $P > 0.05$, *$P < 0.05$, **$P < 0.01$, ***$P < 0.001$).

Downloaded from https://www.pnas.org by KOC UNIVERSITY LIBRARY on June 1, 2026 from IP address 88.255.99.32.

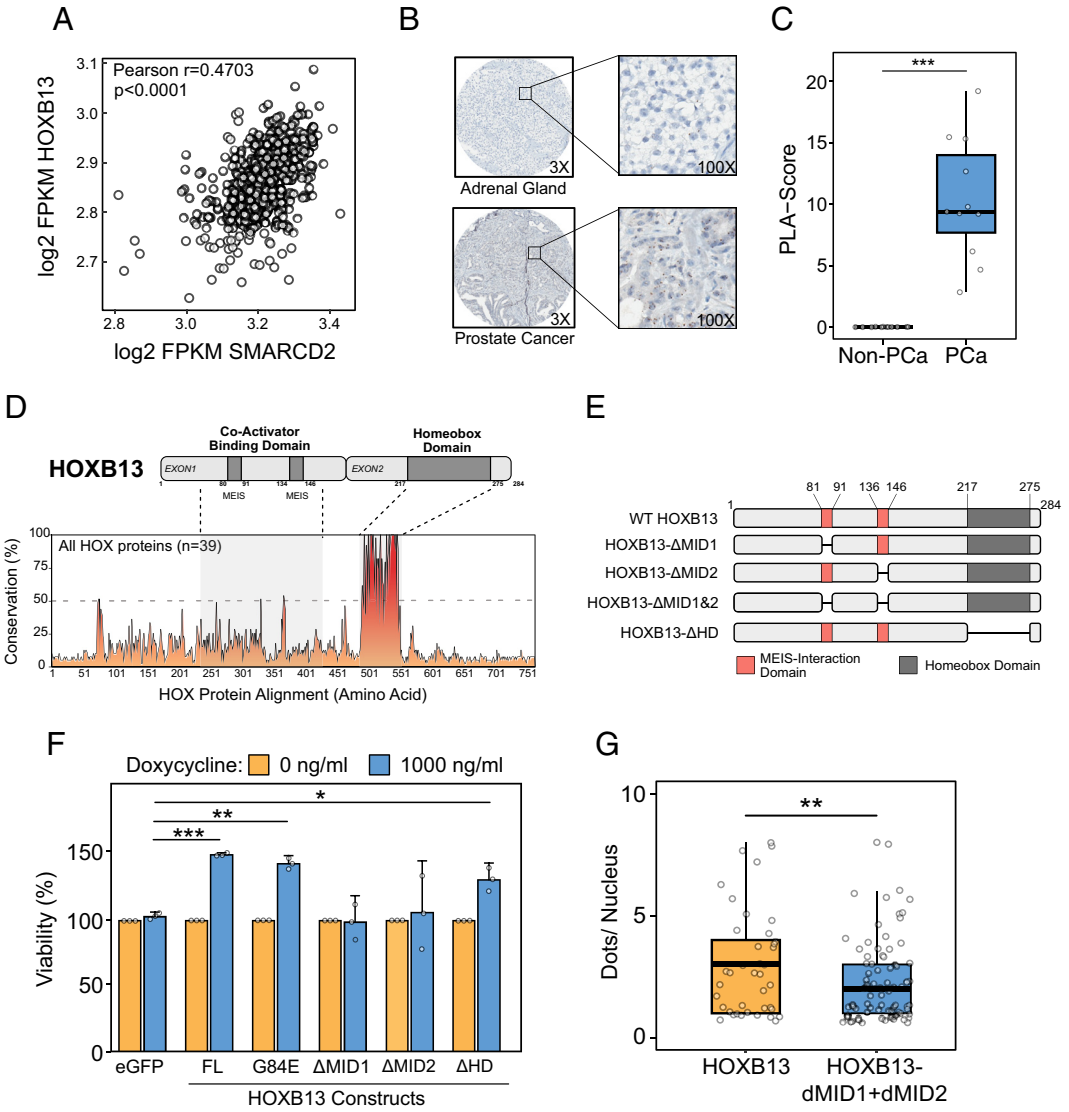


Fig. 6. SMARCD2 interaction with HOXB13 is partially mediated through MEIS interaction domains. (*A*) Expression of *HOXB13* and *SMARCD2* is significantly correlated in the TCGA-PCa cohort. (*B*) HOXB13–SMARCD2 was quantified by PLA in a TMA consisting of normal and cancer samples from both prostate and nonprostatic tissue. Representative images show interactions only in PCa (*Bottom*) but not in the adrenal gland (*Top*). (*C*) Quantification of PLA shows a significant increase in HOXB13–SMARCD2 interactions in PCa compared to non-PCa tissue specimens. (*D*) HOX protein alignment shows two distinct coactivator-binding domains, MEIS-interaction domain-1 (MID1) and MEIS-interaction domain-2 (MID2), and a highly conserved DNA-binding homeobox domain (HD) of *HOXB13*. (*E*) Schematics of various constructs with deleted HOXB13 functional domains. (*F*) Proliferation assay in DU145 with HOXB13 tetracycline-inducible overexpression system demonstrates the essentiality of MEIS-interaction domains for HOXB13 function (n = 3; mean ± SEM). (*G*) DU145-expressing FL-HOXB13 shows significantly more interactions with SMARCD2 compared to MID1 and MID2 deleted HOXB13 (HOXB13 –dMID1 + dMID2) quantified by in situ PLA. For all data ns $P > 0.05$, $^{*}P < 0.05$, $^{**}P < 0.01$, $^{***}P < 0.001$.

Notably, SMARCD2 ChIP-seq in PC3 cells also showed clear co-occupancy with cell-specific HOXB13-binding sites (*SI Appendix*, Fig. S8). Overall, these results suggest that HOXB13 and SMARCD2 co-occupy regulatory elements in both AR-positive and AR-negative PCa. Next, to test whether interactions were stabilized by AR binding, we quantified HOXB13–SMARCD2 PLA in the presence or absence of androgen (DHT). We observed significantly higher PLA signals in those cells treated with DHT as compared to EtOH ($P < 0.0001$; *SI Appendix*, Fig. S9 *A* and *B*). We observed a similar phenotype in AR-negative PCa where knock down of *FOSL2*, a transcription factor subunit of the AP-1 complex, also reduced HOXB13–SMARCD2 interactions (Fig. 5*G* and *SI Appendix*, Fig. S9*C*), suggesting that HOXB13–SMARCD2 interactions were common but distinctly regulated in different stages of PCa. Testing the potential impact of HOXB13 on transcription factor activity (35), we found that overexpression of HOXB13 significantly increased AR-mediated enhancer activity at HOXB13-bound sites but not unbound regions. ($P < 0.001$; *SI Appendix*, Fig. S10). To explore this interaction in a PCa clinical cohort, we analyzed the expression of HOXB13 and SMARCD2, and found that their expression correlated in primary PCa (Fig. 6*A*). To validate HOXB13–SMARCD2 interactions in clinical PCa, we performed PLA on clinical samples and found that HOXB13–SMARCD2 interactions occurred only in the prostate but not in nonprostatic tissue (Fig. 6 *B* and *C*). This HOXB13–SMARCD2 interaction was observed in almost all clinical samples regardless of metastatic potential, Gleason score, or tumor, node, and metastasis (TNM) grading (*SI Appendix*, Fig. S9 *E*–*G*). Taken together, these results suggest that while HOXB13 interacts with unique transcription factors in AR-positive and -negative PCa, interactions with SMARCD2 offer a common effector function.

HOXB13 Interacts with SMARCD2 Through MEIS-Interaction Domains. Having demonstrated HOXB13–SMARCD2 interactions, we then mapped the site of interaction. *HOXB13* encodes two distinct coactivator-binding domains, MEIS-interaction domain-1 (MID1)

Downloaded from https://www.pnas.org by KOC UNIVERSITY LIBRARY on June 1, 2026 from IP address 88.255.99.32.

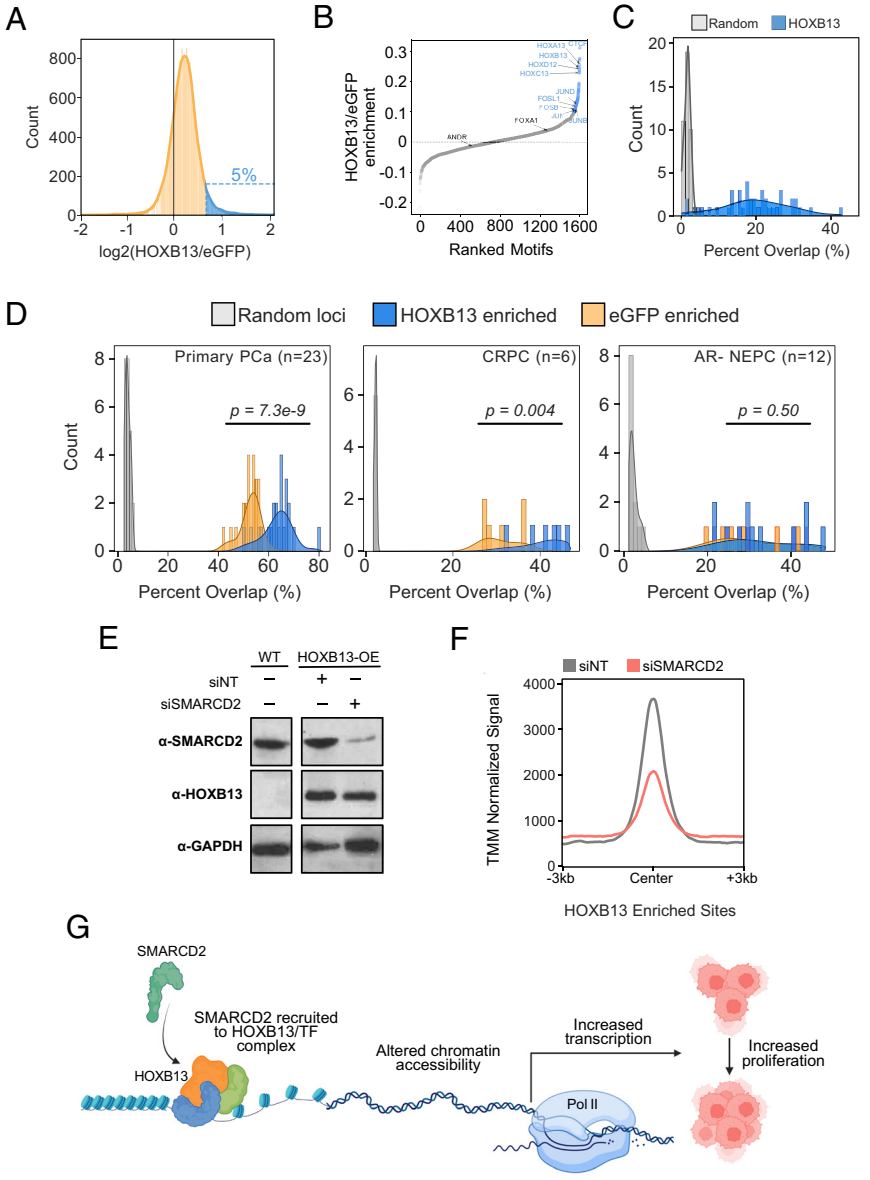


Fig. 7. HOXB13-mediated recruitment of SMARCD2 increases chromatin accessibility. (*A*) ATAC-seq was performed in DU145 cells expressing eGFP or FL-HOXB13. ~ 5% of the accessible chromatin regions (highlighted in blue) are high-confidence HOXB13-specific open chromatin. (*B*) TOBIAS analysis was performed on ATAC-seq data from HOXB13-transfected DU145 cells to identify transcription factor footprints at accessible chromatin regions. After Tn5 bias correction, footprint scores revealed strong enrichment of HOX motifs. Multiple AP-1 factors (JUND, JUN, JUNB, FOSL1, FOSB) showed significant occupancy, while AR and FOXA1 motifs were not enriched despite appearing in initial motif analyses. Blue points indicate significantly enriched motifs in the HOXB13 condition ($P < 1e{-}10$, change > 0.1); selected TFs of interest are labeled. (*C*) A significant overlap was observed for HOXB13-enriched open chromatin regions with clinical HOXB13-binding sites (GSE130408) compared to random regions. (*D*) HOXB13-enriched sites are significantly enriched over random or eGFP at open-chromatin region in primary PCa (*Left* panel), and CRPC (middle panel) but not AR-negative NEPC tissue (*Right* panel) (*E*) siRNA-mediated knockdown of SMARCD2 reduces the expression of SMARCD2 in HOXB13-expressing DU145 cells. No change in HOXB13 expression was observed. (*F*) Loss of SMARCD2 shows a marked reduction in ATAC-seq signal in HOXB13-expressing DU145 cells. (*G*) Schematic representation of the proposed mechanism of HOXB13 in PCa, where the recruitment of SMARCD2 alters chromatin accessibility and increases the transcription of target genes that promote PCa growth.

and MEIS-interaction domain-2 (MID2), and a highly conserved DNA-binding homeobox domain (HD) (Fig. 6*D*). As *HOXB13* overexpression was found to increase proliferation of *HOXB13*-null DU145 (Fig. 2*G*), we conducted a gain-of-function experiment with distinct *HOXB13* mutations/deletions including G84E substitution (an SNP commonly seen in heritable PCa), ΔMID1, ΔMID2, and ΔHD (Fig. 6*E*). No significant differences were observed in mutant HOXB13 protein expression (*SI Appendix*, Fig. S6*F*). When we tested the effects of these mutants on cell proliferation using a tet-inducible expression systems, we found that HOXB13-ΔMID1 and HOXB13-ΔMID2 constructs did not increase DU145 cell proliferation while all other constructs (G84E and ΔHD) increased cell growth at a rate similar to WT HOXB13 (Fig. 6*F*). To determine whether the SMARCD2–HOXB13 interaction occurs through the MID1 and MID2 domains, we conducted HOXB13–SMARCD2 PLA in DU145 cells and observed a significant reduction in HOXB13–SMARCD2 interactions in those cells expressing HOXB13-ΔMID1+ΔMID2 (Fig. 6*G* and *SI Appendix*, Fig. S9*D*). Supporting our findings from the PLA, CoIP of ΔMID1+MID2 variants showed reduced SMARCD2 binding compared to full-length HOXB13 (*SI Appendix*, Fig. S11). However, in both PLA and CoIP, this difference in binding was subtle, suggesting that other HOXB13 domains also interact with SMARCD2. Together, our results indicate that HOXB13 interacts with SMARCD2 partially through its MID1 and MID2, and these domains are essential for HOXB13-mediated activity.

Downloaded from https://www.pnas.org by KOC UNIVERSITY LIBRARY on June 1, 2026 from IP address 88.255.99.32.

HOXB13-Mediated Recruitment of SMARCD2 Increases Chromatin Accessibility. As SMARCD2 is a subunit of chromatin remodeling mSWI/SNF complex, we reasoned that HOXB13 interactions could potentially alter chromatin accessibility. When we characterized ATAC-seq in DU145 cells expressing either eGFP or HOXB13, we saw that HOXB13 expression caused a broad increase in chromatin accessibility at already established euchromatin (Fig. 7*A*). Additional analysis of HOXB13-associated sites from the ATAC-seq data with TOBIAS (36) (Fig. 7*B*) by ranking those transcription factors that were selectively enriched in HOXB13-transfected cells showed that HOX motifs along with a large number of AP-1 members (JUND, FOSL1, FOSB, JUN, and JUNB) were strongly enriched. In contrast, AR and FOXA1 were not significantly enriched, suggesting that these regions are not bound by TFs. Taken together, our data suggest that HOXB13 can bind and increase accessibility at those regions that contain AR or AP-1 motifs but only in AR-negative models does the AP-1 bind to these sites. At HOXB13-enriched sites (top 5%), we saw an increase of motifs associated with HOXB13, AR, and FOXA1 (*SI Appendix*, Fig. S12), and these HOXB13-enriched sites significantly overlapped with clinical HOXB13-binding sites as compared to random sites (Mann–Whitney U P = 1.5e–13) (Fig. 7*C*). To evaluate the clinical relevance of HOXB13-enriched regions, we compared these results with clinical ATAC-seq from both primary PCa (37), CRPC and AR-negative t-NEPC (38) (Fig. 7*D*) and observed a significant overlap in HOXB13-enriched sites as compared to eGFP-enriched or random sites in both primary PCa (p = 7.3e-9) and CRPC (p = 0.004). We did not see significance in AR-negative t-NEPC potentially due to low number of patients or altered HOXB13 cistrome found in AR-negative non-SCL tumors. To determine whether HOXB13-mediated changes in chromatin accessibility occurred via mSWI/SNF recruitment, we characterized if SMARCD2 knockdown altered ATAC-seq in HOXB13 overexpressing cells (Fig. 7*E*). Supporting the proposed mechanism, chromatin accessibility of the HOXB13-enriched regions was significantly decreased by SMARCD2 knockdown (Fig. 7*F*). Together, these findings suggest that HOXB13 alters chromatin accessibility through SMARCD2-mediated activity.

Discussion

HOXB13 is a homeodomain transcription factor that is highly expressed in prostatic tissue and has been previously shown to alter AR DNA binding. Demonstrating the importance of this gene, we found that HOXB13 is essential for the growth of not only AR-positive but also AR-negative PCa models. While several studies have characterized the proliferative impact of HOXB13 in PCa, its role has been contentious with some studies claiming that HOXB13 decreases growth (18, 21), while others show the opposite (39). Our work clearly demonstrates that HOXB13 is selectively essential both in vitro and in vivo for AR-positive and -negative PCa growth. Rapid kinetics of this effect (~4 d) suggests that, in AR-positive PCa cells, this was not solely due to inhibition of AR-mediated transcription as the cytotoxic effect of antiandrogens or AR-degraders typically occurs over a longer time frame (40, 41). Overall, the remarkably selective nature of HOXB13 in PCa, regardless of AR dependency, offers a promising target for future therapeutic interventions.

In both this work and a recent study (22), *HOXB13* was found to be frequently expressed in AR-negative CRPC, suggesting that there may be an AR-independent mechanism of action (Fig. 1 *A*–*D*) (23). Supporting this, we found that the HOXB13 cistrome and interactome are markedly distinct in AR-positive and -negative PCa models. While HOXB13 interacts with AR and constitutively active variants (20) in AR-positive PCa, our work shows that HOXB13 in AR-negative SCL-CRPC interacts with the AP-1 complex. AP-1's role in PCa is complex, as the members Fos and JunB have been proposed to be tumor suppressors that repress advanced disease progression (42). However, there is clear evidence that it is also a major driver in SCL-CRPC transcription (7). HOXB13 is known to change its protein–protein interactions during PCa initiation, and transitions from interacting with tumor suppressor MEIS1 in normal prostatic tissue to the oncogenic AR in primary PCa (15–17). Our results suggest that in AR-negative PCa, HOXB13 once again interacts with a new transcription factor to modulate gene expression. Yet despite these differences in transcription factor interactions, we found that HOXB13 commonly interacts with the mSWI/SNF complex member SMARCD2. The recruitment of SMARCD2 via HOXB13 MID1 and MID2 alters chromatin accessibility and increases tumor proliferation in PCa (Fig. 7*G*). While our data show that HOXB13 HD does not affect the PCa growth, this does not necessarily contradict our genomic findings showing that HOXB13-binding sites are enriched for canonical DNA motifs. Transcription factors frequently bind sites that often do not have motifs as they can be recruited to these regions via indirect mechanisms, including protein–protein interactions or phase-separated transcriptional hubs (19, 43). Our studies in AR-negative SCL support a model in which HOXB13 directly binds to chromatin at AP-1-bound sites in a sequence-specific manner. This complex then recruits SMARCD2 and increases accessibility at bound regulatory elements. The ΔHD overexpression findings in DU145 highlights the context-specific nature of HOXB13 function and suggests that the transcriptional and chromatin-modifying roles may be separable in certain cellular settings. Notably, the common germline variant of *HOXB13*, G84E, was not associated with HOXB13–SMARCD2 interaction either, suggesting that its role in PCa initiation is independent from our observed proliferative phenotype. Considering that the HOXB13–SMARCD2 interaction is highly specific to prostate tissue (Fig. 6*C*) and mSWI/SNF proteins are involved in disease progression (44), this protein interaction may offer a potential pharmacological target in CRPC. However, further mechanistic studies are needed in larger clinical cohorts to better understand this interaction in lethal PCa.

Notably, there are several limitations to this work. Given the robust phenotype we observed on proliferation, we had difficulty characterizing the impact of *HOXB13* knockout on gene expression. While we generated a stable *HOXB13* knockout population, we found that these resistant cells had a markedly different morphology and growth compared to parental cells. Recent studies suggest that these AR-positive *HOXB13*-null cell lines have distinct metabolic activity that occurs through loss of HDAC3 interactions (21). Our findings are distinct as they represent the acute impact of HOXB13 inhibition in PCa. Further, we were limited to characterizing the impact of exogenous *HOXB13* mutant overexpression to DU145 as we observed strong toxicity in HOXB13-dependent LNCaP. However, these experiments support our initial findings that HOXB13 promotes PCa growth and proliferation. Even with noted limitations, our data clearly demonstrate that HOXB13 is a key transcription factor in both AR-positive and -negative PCa.

In conclusion, our study highlights the critical role of HOXB13 in driving both AR-positive and -negative PCa. This work highlights the versatility of HOXB13 in modulating gene expression through interactions with context-specific transcriptional complexes. Yet given the common nature of HOXB13–SMARCD2 interactions and its potential role in CRPC progression, this complex represents a promising therapeutic target in advanced PCa.

Materials and Methods

Cell Culture. LNCaP, PC3, 22Rv1, VCaP, DU145, HEK293T, and Hep3B cell lines were purchased from ATCC and validated by short tandem repeat testing. LNCaP-ABL(45)

Downloaded from https://www.pnas.org by KOC UNIVERSITY LIBRARY on June 1, 2026 from IP address 88.255.99.32.

and LNAI (46) cell lines were a kind gift from Professor Zoran Culig and Professor Paul Rennie. LNCaP cells were cultured in RPMI 1640 with L-glutamine (Lonza #12-702Q) supplemented with 10% tetracycline-free fetal bovine serum (Biowest #S181T) and 1% penicillin/streptomycin (Gibco #15140122). PC3, 22Rv1, DU145, and Hep3B cells were cultured in RPMI 1640 with L-glutamine supplemented with 10% fetal bovine serum (Biowest #S1300) and 1% penicillin/streptomycin. VCaP and HEK293T cells were cultured in DMEM-high glucose (Sigma-Aldrich #D6429) supplemented with 10% fetal bovine serum and 1% penicillin/streptomycin. LNCaP-ABL and LNAI cells were cultured in RPMI 1640 with L-glutamine supplemented with 10% charcoal-stripped fetal bovine serum (Biowest #S181F) and 1% penicillin/streptomycin. All cell lines were regularly tested for *Mycoplasma*.

Plasmids and Cloning. lentiCRISPRv2 (Addgene #52961) was used for CRISPR/Cas9 genome editing. lentiCRISPRv2 vector was digested with BsmBI (NEB #R0580) and dephosphorylated with Antarctic Phosphatase (NEB #M0289S). Annealed sgRNA oligo pairs were phosphorylated with T4 PNK (NEB #M0201S) and ligated with Quick Ligase (NEB #M220S). pLKO_HOXB13_#1 (Addgene #70093) and pLKO_HOXB13_#2 (Addgene #70094) were used for shRNA knockdown. For shRNA control; shFF was cloned into pLKO.1-puro (Addgene #8453). For tet-inducible shRNA knockdown system; shCtrl and shHOXB13 were cloned into Tet-pLKO-puro (Addgene #21915). HOXB13 was PCR amplified from pLX302_HOXB13 (Addgene #70089), digested with SalI/XbaI (NEB #R3138 and #R0145), and ligated into linearized pENTR1A (Addgene #17398). Site-directed mutagenesis was performed to generate mutation constructs. Entry plasmids were recombined to the all-in-one Tet-inducible pLX402 (Addgene #25896) destination vector with Gateway LR Clonase II Enzyme Mix (Invitrogen #11791020). All clonings were validated by Sanger sequencing. gRNA/shRNA sequences are given in *SI Appendix*, Table S1.

Viral Packaging and Titer Calculation. HEK293T cells (2.5×10^6) were seeded on a 100-mm cell culture dish (Corning #430167) 24 h before transfection. Transfer lentiviral plasmids (2,500 ng) were diluted in 200 μl serum-free medium together with 225 ng pCMV-VSV-G (Addgene #8454) and 2,250 ng psPAX2 (Addgene #12260) plasmids. FuGENE 6 transfection reagent (Promega #E2691) diluted in serum-free DMEM was added to plasmid mixture at 1.5:1 (reagent:DNA) ratio. The mixture was incubated at room temperature for 30 min and added to cells dropwise. Cell media were refreshed after 16 h of incubation, and viral supernatant was collected 48 and 72 h after transfection. Viral supernatant was filtered with 0.45 μm syringe filters (Corning #431225) and stored at −80 °C until use. Viruses were titered and used to transduce cells supplemented with 8 μg/ml protamine sulfate (Sigma-Aldrich #P3369).

Proliferation Assay. Cell proliferation was measured by the Cell-Titer Glo (CTG) Luminescent Cell Viability Assay (Promega #G7570), MTS Colorimetric Cell Proliferation Assay (Promega, #G3580), PrestoBlue Cell Viability Reagent (ThermoFisher #A13262), and manual cell counting with a hemocytometer. Cells were seeded in either black 96-well plates (Corning #3603) or transparent 96-well plates (Sarstedt #83.3924) at 2,000 cells/well. Cells were incubated for 96 h and proliferation rates were measured. For the CTG assay, a mixture of 40 μL medium + 4 μL reagent was added, and the relative luminescence was measured using BioTek Synergy H1 Hybrid Multi-Mode Reader (Agilent). For the MTS assay, 20 μL reagent was added and incubated at 37 °C for 2 h. Absorbance was recorded at 490 nm using BioTek Synergy H1 Hybrid Multi-Mode Reader. For the PrestoBlue assay, 10 μL reagent was added and incubated at 37 °C for 1 h. Fluorescence was measured using the TECAN Infinite 500 plate reader. For manual cell counting, 100,000 cells/well were seeded in 6-well plates, and cell numbers were counted with a hemocytometer after 96-hour incubation.

Annexin V & Dead Cell Assay. Programmed cell death was measured by Muse Annexin V & Dead Cell Kit (Cytek #MCH100105). 500 particles/μL were prepared in a mixture of 75 μL Annexin V & Dead Cell Kit reagent and 75 μL 1X DPBS supplemented with 1% FBS. After 20-minute incubation at room temperature in the dark, samples were analyzed using the Muse Cell Analyzer (Cytek). 5000 events were recorded for each set of experiments.

Luciferase Assay. Validated AR enhancers (750 to 850Â bp) were selected for testing based on HOXB13 ChIP-seq and stratified as either "HOXB13 binding low" or "HOXB13 binding high" (*SI Appendix*, Table S2) and assayed with the luciferase reporter assay as previously described (35). Briefly, 293 T cells were cotransfected with 100 ng reporter plasmid, 5 ng of Renilla, 100 ng pEZY_AR plasmid, and either 100 ng pEZY_eGFP or pEZY_Flag_HOXB13 using TransIT-2020 (Mirus #MIR5504), and plated in DMEM + 10% FBS. 48 h posttransfection, cells were treated with 10Â nM of DHT or ETOH for 24Â h. Firefly and Renilla luciferase activity were assayed by the Dual-Glo Luciferase assay system (Promega #E2920). Relative activity was calculated by fixing AR and eGFP-transfected cells at 100%.

In Vivo Animal Studies. In vivo experiments were approved by Koç University Animal Experiments Ethics Committee. LNCaP or PC3 cells were transduced with lentiCRISPRv2-HOXB13_sgRNA #1 or nontargeting sgRNA. LNCaP (3.5×10^6 cells/animal) were mixed with Matrigel hESC-qualified Matrix (Corning #354277) at a 1:1 (vol/vol) and injected subcutaneously into eight male nude mice. PC3 (1.5×10^6 cells/animal) were directly injected subcutaneously into male nude mice (n = 15). Cell viability of HOXB13 knockout cells was confirmed by dye exclusion (trypan blue) prior to injection, and an equal number of viable cells were injected. For tetracycline-inducible experiments, PC3-luciferase cells were transduced with either Tet-pLKO_shHOXB13 #1 or Tet-pLKO_shFF. Following antibiotic selection, cells (1.5×10^6 cells/animal) were injected subcutaneously into male nude mice (n = 20). Once the tumors became palpable, 500 μg doxycycline was injected intraperitoneally on alternate days. Tumor volume was monitored weekly by caliper measurements. Upon completion of the study, tumors were excised and imaged.

Chromatin Immunoprecipitation Sequencing (ChIP-seq). ChIPseq was performed as previously described (47). For the ChIP of SMARCD2 in PC3 cells, double cross-linking was used as described (48). Briefly, 10×10^6 cells were cross-linked with 2 mM disuccinimidyl glutarate (DSG) (ThermoFisher #20593) for 45 min at room temperature followed by 1% formaldehyde (with 10% methanol) cross-linking for 10 min. After lysis and nuclear enrichment, immunoprecipitation was carried out using HOXB13 (Abcam #ab227879), and SMARCD2 (Abcam #ab221168 or # ab220164) -conjugated protein G Dynabeads (Invitrogen #10003D) overnight at 4 °C. After washing, DNA was eluted, de-cross-linked at 65 °C for 8 h, purified using the Monarch DNA purification kit (NEB #T1030), and quantified by the Qubit high-sensitivity DNA kit (Invitrogen #Q33230). DNA (5 ng) was used for sequencing library construction using the NEBNext Ultra II DNA Library Prep Kit for Illumina (NEB #E7645) according to the manufacturer's instructions. The library was amplified for 10 cycles, quantified by Bioanalyzer (Agilent), and sequenced using Illumina NovaSeq 6000 with a minimum of 29 M paired-end reads for each sample.

Assay for Transposase-Accessible Chromatin using sequencing (ATAC-seq). ATAC-seq was performed as described (49) with minor modifications. Briefly, 50,000 live DU145 cells expressing GFP or HOXB13 were lysed in 50 μL cold lysis buffer (10 mM Tris-HCl, pH 7.5, 10 mM NaCl, 3 mM MgCl2, 0.1% NP-40, 0.1% Digitonin, and 0.1% Tween-20) on ice for 3 min. The intact nucleus was tagmented with 2.0 μL of Tn5 Transposase (Illumina #FC-121-1030) and incubated at 37 °C on a thermomixer at 1,000 RPM. DNA was purified by the Minielute reaction cleanup kit (Qiagen #28206), amplified with unique barcoded primers (*SI Appendix*, Table S1), and sequenced using Illumina Novaseq 6000 with a minimum of 30 M reads for each sample.

ChIP-seq and ATAC-seq data analysis. Quality checks of raw and concatenated FASTQ files were done by FastQC (v0.11.9), and compared using MultiQC (v1.11) (50). Paired-end reads were aligned to the hg38 genome build using BWA (v0.7.17-r1188) (51). Duplicate alignments and alignments with a MAPQ score lower than 30 were removed. *ChIPseq:* Binding regions were called with MACS3 (v3.0.0a6) (52). Signal bedgraph files were generated using bedtools (v2.30.0) (53) and converted into bigwig files using bedGraphToBigWig (v4) tool. The signal was TMM normalized (54) with calculated normalization factors using edgeR (v3.36.0) (55). *ATAC-seq:* Mapped mitochondrial DNA was filtered (56), and accessible peaks were called using MACS3 (v3.0.0a6). *Patient ChIPseq:* Raw single end sequencing reads for patient ChIP-seq samples were obtained from GSE130408 and aligned to the hg38 genome build using BWA. Binding regions were called with MACS2 (v2.1.1). All publicly available data are described in *SI Appendix*, Table S3.

Motif Analysis. FIMO (v5.3.0, (57)) was used to identify matches for HOCOMOCO v11 CORE motifs (58). Natural logarithm of q-values was calculated for each motif instance and grouped by each factor for each set to average significance. Differences between average log q-values of each factor between set pairs were calculated and ranked. ATAC-seq data were processed using TOBIAS (36) to assess differential TF footprinting. Tn5 insertion bias was corrected using the ATACorrect module and consistent peak regions across conditions. Corrected bigWig signal

Downloaded from https://www.pnas.org by KOC UNIVERSITY LIBRARY on June 1, 2026 from IP address 88.255.99.32.

tracks were generated for each condition and used as input to FootprintScores module to compute footprint scores across shared ATAC-seq peaks. Differential TF activity was analyzed with the BINDetect module using a curated HOCOMOCO-derived motif database (H13CORE).

RNA-seq Analysis. *AR* and *HOXB13* expressions were quantified from publicly available RNAseq of CRPC (n = 99) patient cohorts (24). Gene Set Variation Analysis (GSVA) was used to calculate published AR and t-NEPC signatures (5). Regularized log-transformed (rlog) RNA-seq expression and ATAC-seq accessibility data were obtained from files with GEO accession GSE181374 and GSE193917, respectively (7). Principal component analysis (PCA) was performed using scikit-learn package, and the top two components were plotted to capture dominant axes of transcriptomic variance. Samples were grouped into four transcriptional subtypes based on prior annotations from the original study: AR+ (G1), WNT (G2), NE (G3), and SCL (G4).

Patient Randomization. Clinical ATAC-seq [CRPC and NEPC: GSE156291, Primary PCa: (37)] and HOXB13 ChIP-seq (GSE130408) were bootstrapped (1,000x) to generate randomized genomic regions with the same size distribution as experimental ATACseq peaks and intersected with clinical ChIP or ATAC narrowPeaks.

Rapid Immunoprecipitation Mass spectrometry of Endogenous protein (RIME). RIME was performed as previously described (59). Briefly, 2×10^7 cells were cross-linked with 1% methanol-free mass spectrometry grade formalin for 8 min at room temperature. After cell lysis and nuclear enrichment, immunoprecipitation was carried out using HOXB13 (Abcam #ab2227879) or IgG (R&D Systems #AB-105-C) -conjugated protein G Dynabeads (Invitrogen #10003D) overnight at 4 °C with rotation. Beads were rigorously washed for 10X with cold RIPA buffer (50 mM HEPES (pH 7.6), 1 mM EDTA, 0.7% (wt/vol) sodium deoxycholate, 1% (vol/vol) NP-40, and 0.5 M LiCl) followed by 2X wash with cold 100 mM ammonium bicarbonate in a protein low-bind tube. Beads were thoroughly dried and stored in −80 °C until trypsin digestion.

Label-Free LC-MS/MS Proteomics. On-bead trypsin digestion was carried out in 50μL HEPES pH 8.0 with 1 μg trypsin at 37 °C overnight. Digested peptide was desalted with C18 TopTips (200μL), lyophilized by Centrivap, and dissolved at 0.7 μg/μL with 0.1% formic acid. Analysis was conducted on Orbitrap Fusion Lumos MS platform (ThermoFisher) coupled to Easy-nLC 1200 system (ThermoFisher) using in-house 100 μm ID × 100 cm column (Dr.Maisch 1.9μ C18) and EasySpray source (ThermoFisher) with a gradient of mobile phase A (water and 0.1% formic acid) and B (80% acetonitrile with 0.1% formic acid) at 0.25 μL/min, 2 to 27%B from 2 to 90 min followed by 27 to 40% B over 12 min, 40-95% B over 8 min and 10 min at 95% B. Data were acquired with a data-dependent method (MS2) in Orbitrap using a positive ion spray (2100v) and default charge state 2. Survey scans (MS1) were acquired at 120 K resolution across a mass range of 350 to 1,500 m/z, with RF 30, an AGC target of 4e5, and a maximum injection time of 50 ms in profile mode. Data files were processed with Protein Discoverer 2.5. Searches were carried out with Sequest HT with SwissProt TaxID = 9606 (v2017-10-25) with precursor mass tolerance 10 ppm and fragment mass tolerance 0.01 Da, carbamidomethyl static modification, K,M,P oxidation, and S,T,Y Phos dynamic modification. Differential enrichment was performed by NormalyzerDE using default parameters (60). The functional role of significantly enriched proteins was determined by Metascape (32). Identified proteins are listed in *SI Appendix*, Table S4.

Proximity Ligation Assay (PLA). PLA was carried out using Duolink® kit (Sigma-Aldrich #DUO92101) according to the manufacturer's instructions. Briefly, cells were fixed with 4% Formalin for 10 min at room temperature and permeabilized with 0.3% TritonX-100. Cells were incubated overnight at 4 °C with anti-HOXB13 (Cell Signaling #90944) or anti-IgG antibody with anti-SMARCD2 (SCBT #sc-101162). Protein–protein interactions were amplified with red fluorescence. Signal was quantified by confocal microscopy (Olympus) under 60X magnification. HOXB13–SMARCD2 interactions in clinical samples were analyzed in a tissue microarray containing 122 prostate specimens (24 benign, 42 localized PCa, and 46 metastatic PCa) and 24 nonprostatic tissue specimens. Duolink® (Sigma-Aldrich #DUO92012) was adapted from the manufacturer's protocol to use on Ventana DISCOVERY Ultra autostainer as described (61). Briefly, antigen was retrieved at 91 °C for 64 min. Tissues were incubated with anti-HOXB13 (Cell Signaling #90944) and anti-SMARCD2 (SCBT #sc-101162) for 12 h at room temperature. After 1-h ligation and 2-h amplification, cells were stained with nuclear staining solution. Protein–protein signal was scanned and scored digitally with Aperio image scope software (Leica Microsystems).

Protein Coimmunoprecipitation. pEzy-Flag-HOXB13 or pEzy-Flag-GFP was cotransfected with pEzy-myc-his-SMARCD2 in HEK293 cells. After 48 h, cells were lysed with ice-cold IP lysis buffer (10 mM Tris-HCl pH 7.4, 10 mM NaCl, 1% Triton X 100, and 1% NP-40). Lysate was incubated with anti-FLAG antibody (Sigma-Aldrich #F1804) -conjugated magnetic beads (Invitrogen #1003D) overnight at 4 °C. After washing with IP buffer (10 mM TRIS HCl pH 7.4, 1 mM EDTA, 150 mM NaCl, 1% TritonX 100), beads were boiled with 1X loading buffer. Protein was run on an SDS PAGE and probed with anti-his antibody (Cell Signaling #2365). For HOXB13ΔM1M2, cells were transfected with 5 μg pEZY-Myc-His-SMARCD2 and 5 μg of pEZY-FLAG-eGFP, pEZY FLAG-HOXB13, or 1.25 μg pEZY-FLAG-HOXB13ΔM1M2 with 3.75 μg pEZY-FLAG-eGFP (due to higher expression levels of ΔM1M2 construct). Immunoprecipitation was performed as previously described (62). Following transfer to a PVDF membrane, the lower portion was probed for HOXB13 (Cell Signaling #90944) while the upper portion was sequentially probed for His-tag (Cell Signaling #2365) and vinculin (SCBT #73614), using anti-rabbit HRP and anti-mouse AlexaFluor680 conjugated secondaries, respectively. Band quantification was performed in ImageJ to measure band intensities and subtract background for each associated lane. Within each set of values, the other two samples were normalized to HOXB13-FL. The relative amount of protein in input was calculated via dividing HOXB13 input values by vinculin loading control values. The relative efficiency of CoIP was calculated via dividing HOXB13 IP values by HOXB13-normalized input values.

Immunohistochemistry (IHC). A tissue microarray containing 139 specimens (35 untreated primary [hormone naive] tumors, 26 NHT tumors, 37 CRPCs, and 41 NEPC) was obtained from Vancouver Prostate Center Tissue Bank. Except for CRPC samples obtained via transurethral resection of the prostate, all specimens were collected through radical prostatectomy. IHC staining was performed with mouse anti-HOXB13 monoclonal antibody (Cell Signaling #90944) using Ventana autostainer (Discover XT from Ventana Medical System) with enzyme-labeled biotin–streptavidin system and solvent-resistant DAB Map kit (Ventana). HOXB13 staining intensity was scored by a clinically trained pathologist. Immunohistochemical assessment of HOXB13 was performed using rabbit monoclonal antibody (Cell Signaling #90944), as previously described (22). For colabeling of HOXB13 with neuroendocrine markers, synaptophysin (SYP; 1:50) (SCBT #SC-17750) and INSM1 (1:50) (SCBT #SC-271408) were used. Immunocomplexes were visualized using the Tyramide Signal Amplification (TSA) system, following the protocols described in (22).

Data, Materials, and Software Availability. Genome binding/occupancy profiling by high throughput sequencing data have been deposited in Gene Expression Omnibus (GEO) [GSE228745 (SuperSeries): (63) GSE228742 (SubSeries-ATAC): (64) GSE228743 (SubSeries-ChIP): (65)].

ACKNOWLEDGMENTS. This work was supported by funding from the Canadian Institute of Health Science (PJT-173331), TUBITAK (221Z116), and PNW SPORE (NIH P50 CA097186). SL was partially supported by a Prostate Cancer Foundation British Columbia PDF fellowship. We gratefully acknowledge the use of the services and facilities of the Koç University Research Center for Translational Medicine (KUTTAM).

Author affiliations: [a]Koç University Research Center for Translational Medicine, Istanbul 34450, Türkiye; [b]Department of Medical Pharmacology, School of Medicine, Koç University, Istanbul 34450, Türkiye; [c]Vancouver Prostate Centre, Vancouver, BC V6H 3Z6, Canada; [d]Department of Urologic Science, University of British Columbia, Vancouver, BC V5Z 1M9, Canada; [e]Center for Functional Cancer Epigenetics, Dana-Farber Cancer Institute, Boston, MA 02215; [f]Division of Oncogenomics, Oncode Institute, Netherlands Cancer Institute, Amsterdam 1066 CX, The Netherlands; [g]Laboratory of Chemical Biology and Institute for Complex Molecular Systems, Department of Biomedical Engineering, Eindhoven University of Technology, Eindhoven 5612 AJ, The Netherlands; [h]Division of Clinical Research, Fred Hutchinson Cancer Center, Seattle, WA 98109; [i]Division of Human Biology, Fred Hutchinson Cancer Center, Seattle, WA 98109; and [j]Department of Laboratory Medicine and Pathology, University of Washington, Seattle, WA 98115

Downloaded from https://www.pnas.org by KOC UNIVERSITY LIBRARY on June 1, 2026 from IP address 88.255.99.32.

1. R. L. Siegel, K. D. Miller, A. Jemal, Cancer statistics, 2020. *CA Cancer J. Clin.* **70**, 7–30 (2020).
2. M. A. Eisenberger *et al.*, Bilateral orchiectomy with or without flutamide for metastatic prostate cancer. *N. Engl. J. Med.* **339**, 1036–1042 (1998).
3. E. D. Crawford *et al.*, A controlled trial of leuprolide with and without flutamide in prostatic carcinoma. *N. Engl. J. Med.* **321**, 419–424 (1989).
4. R. Su *et al.*, Comprehensive analysis of androgen receptor status in prostate cancer with neuroendocrine differentiation. *Front. Oncol.* **12**, 955166 (2022).
5. E. G. Bluemn *et al.*, Androgen receptor pathway-independent prostate cancer is sustained through FGF signaling. *Cancer Cell* **32**, 474–489.e6 (2017).
6. R. Aggarwal *et al.*, Clinical and genomic characterization of treatment-emergent small-cell neuroendocrine prostate cancer: A multi-institutional prospective study. *J. Clin. Oncol.* **36**, 2492–2503 (2018).
7. F. Tang *et al.*, Chromatin profiles classify castration-resistant prostate cancers suggesting therapeutic targets. *Science* **376**, eabe1505 (2022).
8. L. Zeltser, C. Desplan, N. Heintz, Hoxb-13: A new Hox gene in a distant region of the HOXB cluster maintains colinearity. *Development* **122**, 2475–2484 (1996).
9. T. Sreenath, A. Orosz, K. Fujita, C. J. Bieberich, Androgen-independent expression of hoxb-13 in the mouse prostate. *Prostate* **41**, 203–207 (1999).
10. K. D. Economides, M. R. Capecchi, *Hoxb13* is required for normal differentiation and secretory function of the ventral prostate. *Development* **130**, 2061–2069 (2003).
11. R. Na *et al.*, The HOXB13 variant X285K is associated with clinical significance and early age at diagnosis in African American prostate cancer patients. *Br. J. Cancer* **126**, 791–796 (2022).
12. J. Gudmundsson *et al.*, A study based on whole-genome sequencing yields a rare variant at 8q24 associated with prostate cancer. *Nat. Genet.* **44**, 1326–1329 (2012).
13. S. Maia *et al.*, Identification of two novel HOXB13 germline mutations in Portuguese prostate cancer patients. *PLoS One* **10**, 1–16 (2015).
14. C. M. Ewing *et al.*, Germline mutations in *HOXB13* and prostate-cancer risk. *N. Engl. J. Med.* **366**, 141–149 (2012).
15. C. VanOpstall *et al.*, MEIS-mediated suppression of human prostate cancer growth and metastasis through HOXB13-dependent regulation of proteoglycans. *Elife* **9**, e53600 (2020).
16. D. Johng *et al.*, *HOXB13* interaction with *MEIS1* modifies proliferation and gene expression in prostate cancer. *Prostate* **79**, 414–424 (2019).
17. R. R. Bhanvadia *et al.*, MEIS1 and MEIS2 expression and prostate cancer progression: A role for *HOXB13* binding partners in metastatic disease. *Clin. Cancer Res.* **24**, 3668–3680 (2018).
18. J. D. Norris *et al.*, The homeodomain protein HOXB13 regulates the cellular response to androgens. *Mol. Cell* **36**, 405–416 (2009).
19. M. M. Pomerantz *et al.*, The androgen receptor cistrome is extensively reprogrammed in human prostate tumorigenesis. *Nat. Genet.* **47**, 1346–1351 (2015).
20. Z. Chen *et al.*, Diverse AR-V7 cistromes in castration-resistant prostate cancer are governed by HoxB13. *Proc. Natl. Acad. Sci. U.S.A.* **115**, 6810–6815 (2018).
21. X. Lu *et al.*, *HOXB13* suppresses de novo lipogenesis through *HDAC3*-mediated epigenetic reprogramming in prostate cancer. *Nat. Genet.* **54**, 670–683 (2022).
22. R. A. Patel *et al.*, Characterization of HOXB13 expression patterns in localized and metastatic castration-resistant prostate cancer. *J. Pathol.* **262**, 105–120 (2023), 10.1002/path.6216.
23. S. Cheng *et al.*, Neuroendocrine prostate cancer has distinctive, non-prostatic HOX code that is represented by the loss of HOXB13 expression. *Sci. Rep.* **11**, 2778 (2021).
24. D. A. Quigley *et al.*, Genomic hallmarks and structural variation in metastatic prostate cancer. *Cell* **174**, 758–769.e9 (2018).
25. Y.-R. Kim *et al.*, *HOXB13* promotes androgen independent growth of *LNCaP* prostate cancer cells by the activation of *E2F* signaling. *Mol. Cancer* **9**, 124 (2010).
26. L. Huang, Y. Pu, D. Hepps, D. Danielpour, G. S. Prins, Posterior Hox gene expression and differential androgen regulation in the developing and adult rat prostate lobes. *Endocrinology* **148**, 1235–1245 (2007).
27. R. P. McMullin *et al.*, A FOXA1-binding enhancer regulates Hoxb13 expression in the prostate gland. *Proc. Natl. Acad. Sci.* **107**, 98–103 (2010).
28. A. Tsherniak *et al.*, Defining a cancer dependency map. *Cell* **170**, 564–576.e16 (2017).
29. C. Jung *et al.*, *HOXB13* is downregulated in colorectal cancer to confer *TCF4*-mediated transactivation. *Br. J. Cancer* **92**, 2233 (2005).
30. R. M. Layer *et al.*, Giggle: A search engine for large-scale integrated genome analysis. *Nat. Methods* **15**, 123–126 (2018).
31. R. Rezsohazy, A. J. Saurin, C. Maurel-Zaffran, Y. Graba, Cellular and molecular insights into Hox protein action. *Development* **142**, 1212–1227 (2015).
32. Y. Zhou *et al.*, Metascape provides a biologist-oriented resource for the analysis of systems-level datasets. *Nat. Commun.* **10**, 1523 (2019).
33. W. Wang *et al.*, Purification and biochemical heterogeneity of the mammalian SWI-SNF complex. *EMBO J.* **15**, 5370–5382 (1996).
34. Y. Yin *et al.*, Impact of cytosine methylation on DNA binding specificities of human transcription factors. *Science* **2239**, 1–15 (2017).
35. C.-C.F. Huang *et al.*, Functional mapping of androgen receptor enhancer activity. *Genome Biol.* **22**, 149 (2021).
36. M. Bentsen *et al.*, ATAC-seq footprinting unravels kinetics of transcription factor binding during zygotic genome activation. *Nat. Commun.* **11**, 4267 (2020).
37. M. R. Corces *et al.*, The chromatin accessibility landscape of primary human cancers. *Science* **362**, eaav1898 (2018).
38. P. Cejas *et al.*, Subtype heterogeneity and epigenetic convergence in neuroendocrine prostate cancer. *Nat. Commun.* **12**, 5775 (2021).
39. C. Jung, R.-S. Kim, H.-J. Zhang, S.-J. Lee, M.-H. Jeng, HOXB13 induces growth suppression of prostate cancer cells as a repressor of hormone-activated androgen receptor signaling. *Cancer Res.* **64**, 9185–9192 (2004).
40. X. Liao, S. Tang, J. B. Thrasher, T. L. Griebling, B. Li, Small-interfering RNA–induced androgen receptor silencing leads to apoptotic cell death in prostate cancer. *Mol. Cancer Ther.* **4**, 505–515 (2005).
41. C. Tran *et al.*, Development of a second-generation antiandrogen for treatment of advanced prostate cancer. *Science* **324**, 787–790 (2009).
42. M. Riedel *et al.*, Targeting AP-1 transcription factors by CRISPR in the prostate. *Oncotarget* **12**, 1956–1961 (2021).
43. A. Boija *et al.*, Transcription factors activate genes through the phase-separation capacity of their activation domains. *Cell* **175**, 1842–1855.e16 (2018).
44. I. E. Ertl *et al.*, The SMARCD family of SWI/SNF accessory proteins is involved in the transcriptional regulation of androgen receptor-driven genes and plays a role in various essential processes of prostate cancer. *Cells* **12**, 124 (2022).
45. Z. Culig *et al.*, Switch from antagonist to agonist of the androgen receptor bicalutamide is associated with prostate tumour progression in a new model system. *Br. J. Cancer* **81**, 242–251 (1999).
46. J. R. Graff *et al.*, Increased AKT activity contributes to prostate cancer progression by dramatically accelerating prostate tumor growth and diminishing p27(Kip1) expression. *J. Biol. Chem.* **275**, 24500–24505 (2000).
47. K. A. Holmes, G. D. Brown, J. S. Carroll, Chromatin immunoprecipitation-sequencing (ChIP-seq) for mapping of estrogen receptor-chromatin interactions in breast cancer. *Methods Mol. Biol.* **1366**, 79–98 (2016).
48. B. Gokbayrak *et al.*, Identification of selective SWI/SNF dependencies in enzalutamide-resistant prostate cancer. *Commun. Biol.* **8**, 169 (2025).
49. M. R. Corces *et al.*, An improved ATAC-seq protocol reduces background and enables interrogation of frozen tissues. *Nat. Methods* **14**, 959–962 (2017).
50. P. Ewels, M. Magnusson, S. Lundin, M. Käller, MultiQC: Summarize analysis results for multiple tools and samples in a single report. *Bioinformatics* **32**, 3047–3048 (2016).
51. H. Li, R. Durbin, Fast and accurate short read alignment with Burrows-Wheeler transform. *Bioinformatics* **25**, 1754–1760 (2009).
52. Y. Zhang *et al.*, Model-based analysis of ChIP-Seq (MACS). *Genome Biol.* **9**, R137 (2008).
53. A. R. Quinlan, I. M. Hall, BEDtools: A flexible suite of utilities for comparing genomic features. *Bioinformatics* **26**, 841–842 (2010).
54. M. D. Robinson, A. Oshlack, A scaling normalization method for differential expression analysis of RNA-seq data. *Genome Biol.* **11**, R25 (2010).
55. M. D. Robinson, D. J. McCarthy, G. K. Smyth, edgeR: A Bioconductor package for differential expression analysis of digital gene expression data. *Bioinformatics* **26**, 139–140 (2010).
56. J. D. Buenrostro, P. G. Giresi, L. C. Zaba, H. Y. Chang, W. J. Greenleaf, Transposition of native chromatin for fast and sensitive epigenomic profiling of open chromatin, DNA-binding proteins and nucleosome position. *Nat. Methods* **10**, 1213–1218 (2013).
57. C. E. Grant, T. L. Bailey, W. S. Noble, FIMO: Scanning for occurrences of a given motif. *Bioinformatics* **27**, 1017–1018 (2011).
58. I. V. Kulakovskiy *et al.*, HOCOMOCO: Towards a complete collection of transcription factor binding models for human and mouse via large-scale ChIP-Seq analysis. *Nucleic Acids Res.* **46**, D252–D259 (2018).
59. H. Mohammed *et al.*, Rapid immunoprecipitation mass spectrometry of endogenous proteins (RIME) for analysis of chromatin complexes. *Nat. Protoc.* **11**, 316–326 (2016).
60. J. Willforss, A. Chawade, F. Levander, NormalyzerDE: Online tool for improved normalization of omics expression data and high-sensitivity differential expression analysis. *J. Proteome Res.* **18**, 732–740 (2019).
61. F. Zhang *et al.*, Dynamic phase separation of the androgen receptor and its coactivators key to regulate gene expression. *Nucleic Acids Res.* **51**, 99–116 (2023).
62. X.-H. Wang *et al.*, The BAG-1 cochaperone is a negative regulator of p73-dependent transcription. *Br. J. Cancer.* **100**, 1347–1357 (2009).
63. B. Ersoy-Fazlioglu *et al.*, HOXB13 alters chromatin accessibility in prostate cancer through interactions with the SWI/SNF complex. Gene Expression Omnibus (GEO). https://www.ncbi.nlm.nih.gov/geo/query/acc.cgi?acc=GSE228745. Deposited 2 April 2023.
64. B. Ersoy-Fazlioglu *et al.*, HOXB13 alters chromatin accessibility in prostate cancer through interactions with the SWI/SNF complex [ATAC-seq]. Gene Expression Omnibus (GEO). https://www.ncbi.nlm.nih.gov/geo/query/acc.cgi?acc=GSE228742. Deposited 2 April 2023.
65. B. Ersoy-Fazlioglu *et al.*, HOXB13 alters chromatin accessibility in prostate cancer through interactions with the SWI/SNF complex [ChIP-seq]. Gene Expression Omnibus (GEO). https://www.ncbi.nlm.nih.gov/geo/query/acc.cgi?acc=GSE228743. Deposited 2 April 2023.

Downloaded from https://www.pnas.org by KOC UNIVERSITY LIBRARY on June 1, 2026 from IP address 88.255.99.32.